Advances in Applied Mathematics and Mechanics
Adv. Appl. Math. Mech., Vol. **9**, No. 5, pp. 1271-1288

DOI: 10.4208/aamm.OA-2016-0103
October 2017

Transition Flow with an Incompressible Lattice Boltzmann Method

J. R. Murdock*, J. C. Ickes and S. L. Yang

Department of Mechanical Engineering-Engineering Mechanics, Michigan Technological University, 1400 Townsend Drive, Houghton, MI 49931, USA

Received 24 August 2016; Accepted (in revised version) 28 March 2017

Abstract. Direct numerical simulations of the transition process from steady laminar to chaotic flow are considered in this study with the relatively new incompressible lattice Boltzmann equation. Numerically, a multiple relaxation time fully incompressible lattice Boltzmann equation is implemented in a 2D driven cavity. Spatial discretization is 2nd-order accurate, and the Kolmogorov length scale estimation based on Reynolds number (*Re*) dictates grid resolution. Initial simulations show the method to be accurate for steady laminar flows, while higher *Re* simulations reveal periodic flow behavior consistent with an initial Hopf bifurcation at *Re* 7,988. Non-repeating flow behavior is observed in the phase space trajectories above *Re* 13,063, and is evidence of the transition to a chaotic flow regime. Finally, flows at Reynolds numbers above the chaotic transition point are simulated and found with statistical properties in good agreement with literature.

AMS subject classifications: 65M10, 78A48

Key words: Multiple relaxation time, lattice Boltzmann, transition, high Reynolds number flow, incompressible flow, lid driven cavity.

1 Introduction

Characteristics of flow transition from steady state to transience and from transience to self-sustaining chaos and instability is an active area of research. While transition to chaos (turbulence in 3D) and separation remain unsolved problems in engineering flow analysis, direct numerical simulation (DNS) work continues to provide insight to the physics in an effort to develop improved turbulence transition and separation models. Past application of the lattice Boltzmann method to chaos and turbulence simulation, such as channel flow by Lammers et al., suffered from the compressibility error [11, 15] inherent in the standard lattice Boltzmann equation [8, 20]. This work extends the study

*Corresponding author.
Email: jrmurdoc@mtu.edu (J. R. Murdock), ickesjc@gmail.com (J. C. Ickes), slyang@mtu.edu (S. L. Yang)

 ©2017 Global Science Press

https://doi.org/10.4208/aamm.OA-2016-0103 Published online by Cambridge University Press

of transitional flow states using an incompressible lattice Boltzmann method (iLBM) and a Multiple Relaxation Time (MRT) collision operator. Although physical turbulence is a three dimensional phenomenon, solutions to the flow equations in two dimensions can exhibit similar randomness.

Bifurcations, chaos, and energy dissipation, among other characteristics, exist, while vortex stretching is absent. With this in mind, this work provides a numerical solution benchmark using MRT-iLBM for comparison with past 2D work.

The Lattice Boltzmann Method (LBM) is a relative newcomer in the field of Computational Fluid Dynamics (CFD), having been first described in 1988 [16]. This class of analysis methodology can take many forms. For continuum flow analysis, parameters are chosen such that numerical solutions to the Navier-Stokes equations are recovered through solving the discrete Boltzmann equation. While the behavior of Navier-Stokes is replicated by LBM, the underlying solver algorithms for LBM are considerably simpler than an equivalent Navier-Stokes solver. Reduced computations-per step reduce overall roundoff error and make the MRT-iLBM a less numerically noisy solution method [10].

Lid-driven cavity flow (LDC) is a canonical flow case useful in evaluating methodology [4]. Literature reporting results for steady and transient laminar, transitional, and chaotic flows using a wide variety of methods is extensive. The complexity of the flow despite simple boundaries, along with the plethora of results, makes it an excellent verification tool. Steady state results were obtained by Ghia et al. [6] using a vorticity-stream function approach up to moderate Reynolds numbers. More recently, fine-grid results were reported by Marchi et al. [13] using finite volume Navier-Stokes. LBM has been applied to the LDC flow in the past by Hou et al. [9], who point out the compressibility error present in their results.

Past studies of 2D driven cavity flow have reported various values for the Reynolds number at the onset of transient behavior, dependent on the balance of noisiness and dissipation of the numerical method used. Cazemier et al. [5] analyzed this flow using both DNS and a reduced-order model deduced from Proper Orthogonal Decomposition of a DNS simulation performed at *Re* 22,000. Peng et al. [18] reported the Reynolds numbers of the first Hopf bifurcation and the turbulence transition, but the sixth order numerical method applied in the domain center was contaminated by larger error terms from the second order spatial scheme applied at the boundaries. It is possible that numerical noise from the combination of low-order accurate numerics and typical grid resolution at the walls - where the highest gradients occur - served as a source of artificial excitation and contributed error to the determination of transitional *Re*. Marie et al. [14] show the dispersion and diffusion error of LBM to be excellent across all wavenumbers, suggesting it is well-suited for DNS analysis.

Several authors report steady solutions of the 2D lid driven cavity flow at Reynolds numbers upwards of 30,000 by omitting time dependency terms in the modeled equations. Failure of these simulations to allow solution unsteadiness belies the fact that the existence of steady flow depends upon Reynolds number-dependent stability criteria. Solution unsteadiness below *Re* 10,000 has been well established since at least the work

https://doi.org/10.4208/aamm.OA-2016-0103 Published online by Cambridge University Press

of Cazemier et al. [5].

The objectives of this work are to establish the MRT-iLBM method as an accurate approach for DNS and compute critical low- to moderate-Reynolds number results using the method. These objectives will be accomplished by first verifying the MRT-iLBM method by showing agreement with literature results for steady, laminar 2D LDC flow. Subsequent objectives include identifying the Reynolds number of the first Hopf bifurcation (the onset of transience) and the Reynolds number of the transition to self-sustaining chaos, respectively, and compare with literature results. Lastly, MRT-iLBM results of DNS at two chaotic Reynolds numbers are reported. Statistical results for these simulations are compared with literature; they are informative about the flow structure but also demonstrate the ability of MRT-iLBM to be effective for performing DNS.

2 Incompressible multiple relaxation time lattice Boltzmann equation

The standard and incompressible lattice Boltzmann equation (LBE) have the same basic form:

$$f_i(\boldsymbol{x}+\delta\boldsymbol{x},t+\delta t)=f_i(\boldsymbol{x},t)-\frac{1}{\tau}\left(f_i-f_i^{eq}\right), \tag{2.1}$$

where f_i are the probability distributions of discrete velocity space, τ is the collision relaxation time, and f_i^{eq} is the equilibrium distribution [8].

Whether one arrives at a compressible flow in the incompressible limit, or a truly incompressible flow depends on the equilibrium distribution term [20]. In the standard LBE this term takes the form:

$$f_i^{eq}=\omega_i\rho\left(1+\frac{\boldsymbol{c}_i\cdot\boldsymbol{u}}{c_s^2}+\frac{(\boldsymbol{c}_i\cdot\boldsymbol{u})^2}{2c_s^4}-\frac{(\boldsymbol{u}\cdot\boldsymbol{u})}{2c_s^2}\right), \tag{2.2}$$

where $\boldsymbol{c}_i$ are the lattice velocities vector, $\boldsymbol{u}$ is the flow velocity vector, ρ is the density, ω_i are the distribution weights, and c_s is the speed of sound for a given lattice. For flows utilizing this formulation, the pressure is defined as $P=c_s^2\rho$, and the relaxation time is related to the kinematic viscosity as $\nu=c_s^2\left(\tau-\frac{1}{2}\right)\delta t$ [8].

The following mass and momentum conservation laws are then satisfied:

$$\sum_i f_i=\rho, \quad \sum_i \boldsymbol{c}_i f_i=\rho\boldsymbol{u}. \tag{2.3}$$

For this study, 2D physics is simulated with nine discrete velocities abbreviated as D2Q9. Fig. 1 graphically demonstrates the D2Q9 lattice. The velocity vectors are then:

$$c_x=\{0,1,0,-1,0,1,-1,-1,1\}, \quad c_y=\{0,0,1,0,-1,1,1,-1,-1\}. \tag{2.4}$$

Weights ω_i correlate inversely with magnitude of each vector:

$$\omega_0=\frac{4}{9}, \quad \omega_{1,2,3,4}=\frac{1}{9}, \quad \omega_{5,6,7,8}=\frac{1}{36}. \tag{2.5}$$

https://doi.org/10.4208/aamm.OA-2016-0103 Published online by Cambridge University Press

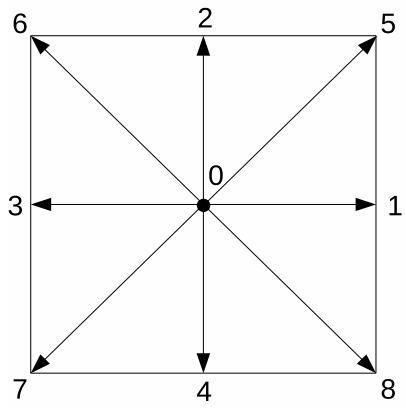


Figure 1: D2Q9 lattice structure.

To resolve the issue of compressibility present in the standard LBE, the equilibrium distribution can be modified by replacing the conservation equations of formulation (2.3) with [7,17,20]:

$$\sum_i f_i = Constant, \quad \sum_i \boldsymbol{c}_i f_i = \boldsymbol{u}, \quad \boldsymbol{uu} + \frac{P}{\rho_0}\boldsymbol{I} = \sum_i \boldsymbol{c}_i \boldsymbol{c}_i f_i, \tag{2.6}$$

and with *Constant* set to 0, the equilibrium distribution function becomes:

$$f_i^{eq} = \begin{cases} -\frac{5}{3}\frac{1}{c^2}P + S_i & \text{for } i=0, \\ \frac{1}{3}\frac{1}{c^2}P + S_i & \text{for } i=1,2,3,4, \\ \frac{1}{12}\frac{1}{c^2}P + S_i & \text{for } i=5,6,7,8, \end{cases} \tag{2.7a}$$

$$S_i = \omega_i \left[3\frac{(\boldsymbol{c}_i \cdot \boldsymbol{u})}{c} + \frac{9}{2}\frac{(\boldsymbol{c}_i \cdot \boldsymbol{u})^2}{c^2} - \frac{3}{2}\frac{(\boldsymbol{u} \cdot \boldsymbol{u})}{c^2} \right], \tag{2.7b}$$

which recovers the fully incompressible hydrodynamic equations for the D2Q9 case and yields for the lattice speed and kinematic viscosity $c = \delta x/\delta t$ and $\nu = \frac{c^2}{3}\left(\tau - \frac{1}{2}\right)\delta t$, respectively. Pressure is calculated from:

$$P = \frac{3c^2}{5}\left[\sum_{i=1}^{8} f_i + S_0 \right]. \tag{2.8}$$

LBM fundamentals presented thus far have utilized the single relaxation time (SRT) Bhatnagar-Gross-Krook (BGK) collision model [1]. With increasing *Re*, stability and boundary location become problematic in the SRT-LBE [2]. While instability is reduced

https://doi.org/10.4208/aamm.OA-2016-0103 Published online by Cambridge University Press

with the iLBE, a multiple relaxation time form further improves LBM for transitional and chaotic flows, as in this study. The MRT-iLBE is expressed as:

$$f_i(\boldsymbol{x}+\delta\boldsymbol{x},t+\delta t)=f_i(\boldsymbol{x},t)-\sum_j \Lambda_{ij}(f_j-f_j^{eq}), \tag{2.9}$$

with Λ_{ij} replacing the inverse SRT value, $\frac{1}{\tau}$. Several values of the new collision matrix are functions of τ. Computations actually occur in moment space, in which each moment has a physical correlation, and are then transformed back to velocity space for macroscopic meaning. Appendix A contains the derivation and complete components of the MRT-iLBE used for this study.

3 Simulation parameters

The lid driven cavity configuration as simulated in this work is shown in Fig. 2. The four walls of the cavity were treated with second order accurate halfway bounce back (HBB) boundary conditions [21]. Simulation similarity is governed by Reynolds number *Re* shown in Eq. (3.1a). Characteristic time t_c is computed according to Eq. (3.1b). These relations contain symbols for wall velocity ($\boldsymbol{u}_{wall}$) and kinematic viscosity (ν). The subscript *lb* signifies that the value used is in lattice Boltzmann units. Numbers presented throughout this work are nondimensional unless otherwise indicated

$$Re=\frac{\boldsymbol{u}_{wall,lb}L_{lb}}{\nu_{lb}}, \tag{3.1a}$$

$$t_c=\frac{L_{lb}}{\boldsymbol{u}_{wall,lb}}. \tag{3.1b}$$

Since the numerics employed are second order both at the boundaries and domain interior, flow feature resolution for this DNS simulation is dependent upon high lattice site counts. This contrasts with the use of larger grid spacing and a higher order spatial differencing based on the flow solution following a given polynominal order between the nodes. Kolmogorov's theory of turbulent length scales is the basis for discretizing each direction by $Re^{0.75}$ lattice sites as the standard grid sizing used in this work, including flow in the laminar regime. The accuracy of this approximation is reported upon with the results of the chaotic flows at *Re* 15,000 and *Re* 20,000. A grid dependence check at *Re* 1,000 is done to show that the MRT-iLBM method is comparable to literature results at lower spatial resolution.

All simulations were started from at-rest initial conditions. As such, there was a burn-in period during which the mean flow values changed as the flow reached a steady state or quasi-steady oscillatory condition. All data presented in this work was taken after the burn-in time was complete.

User specified Reynolds numbers and grid sizes were used to determine the requisite kinematic viscosity according to Eq. (3.1a). Wall velocity was held at the constant value of 0.1 throughout these simulations.

https://doi.org/10.4208/aamm.OA-2016-0103 Published online by Cambridge University Press

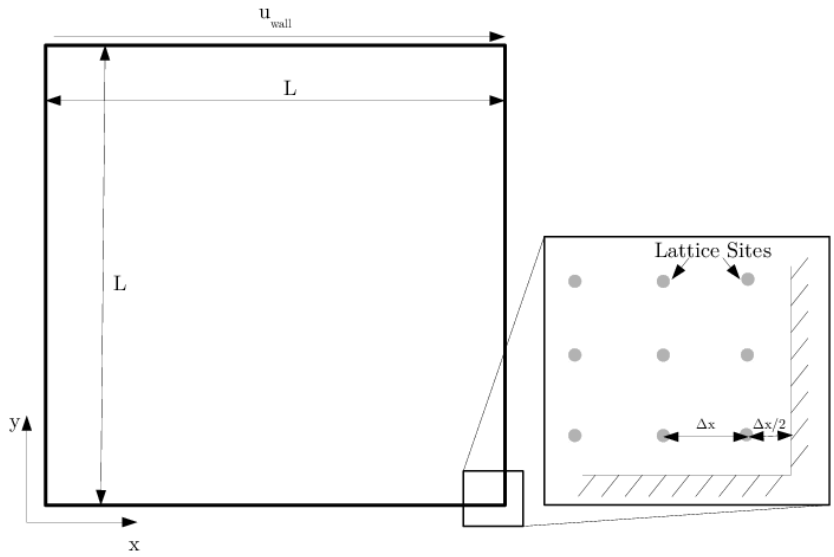


Figure 2: Lid driven cavity simulation setup and detail of HBB boundary condition.

Low Reynolds numbers with steady results (Re 100, 400, 1,000) were simulated to validate the MRT-iLBM code. Comparison of these steady results with literature are given in the Results section. The first Hopf bifurcation was identified by interpolating from transient result data from Reynolds numbers just above the bifurcation Re. To determine the Reynolds number of the transition to chaos, one non-random transient Reynolds number and one chaotic (random and transient) Reynolds number were found, and then a binary search was performed successively until the desired accuracy was achieved. Fully chaotic results were then generated at two higher Reynolds numbers to provide DNS data for the statistical analysis.

3.1 Post processing

Statistical properties of the chaotic flows are generated by a series of post-processing codes which made computations from sets of both macroscopic (u, v) and mesoscopic (f_i) data which were output periodically as the MRT-iLBM code ran. Data included in the statistics met two conditions. First, the mean values of the code were required to be in a steady state which only existed beyond a minimum *burn-in time*. Second, the frequency of data output was required to be adequate to capture the highest frequency components of the system response and not produce aliasing.

Mean velocities are computed by averaging each of the i velocity components, whose instantaneous value is written U_i, at each time step k (N total) for all flow snapshots available. Eq. (3.2a) describes the average for U_i and the pressure P, which has an analogous computation. The square of the fluctuating i^{th} velocity component of velocity u_i^2 is

https://doi.org/10.4208/aamm.OA-2016-0103 Published online by Cambridge University Press

computed from the mean and the available snapshot data

$$\langle U_i \rangle = \frac{1}{N}\sum_k^N U_i^k, \qquad \langle P_i \rangle = \frac{1}{N}\sum_k^N P^k, \tag{3.2a}$$

$$\langle u_i^2 \rangle = \frac{1}{N}\sum_k^N \left(U_i^k - \langle U_i \rangle\right)^2, \qquad AR = \sqrt{\frac{\langle u_1^2 \rangle}{\langle u_2^2 \rangle}}. \tag{3.2b}$$

To assess the anisotropy in the chaotic flows, the ratio of RMS components of fluctuating velocity was computed per Eq. (3.2b). This quantity is referred to as the anisotropy ratio, AR. According to the definition, AR is the multiplier between RMS fluctuating velocity in the x direction and RMS fluctuating velocity in the y direction; and shows how various regions of the flow field are dominated by one fluctuating velocity component or the other.

Local strain rate tensor components S_{ij} were computed based on the work of Li and Wang [12]. Namely, the mesoscopic properties of the flow were incorporated into the components of the 2D strain rate tensor as shown in Eq. (3.3a). Data files periodically output by the code contained instantaneous snapshots of the strain rate tensor field at each lattice site in the domain. A code was run post-process to compute the mean and the mean fluctuating components of the strain rate tensor, $\langle S_{ij} \rangle$ and s_{ij}, respectively. What we will call the turbulence kinetic energy dissipation ϵ for 2D flows, was computed according to Eq. (3.3b)

$$S_{ij} \approx \frac{-3}{2\rho c^2 \tau \Delta t}\sum_\alpha c_{i,\alpha} c_{j,\alpha}\left(f_{post,\alpha} - f_\alpha^{eq}\right), \tag{3.3a}$$

$$\epsilon = 2\nu \langle s_{ij} s_{ij} \rangle. \tag{3.3b}$$

Kolmogorov length scale was computed for each lattice site in the domain according to the relation given in Eq. (3.4). η_k quantifies the spatial resolution of the simulation; values less than one indicate that the smallest and shortest-lived flow features are not fully captured

$$\eta_k = \left(\frac{\nu^3}{\epsilon}\right)^{\frac{1}{4}}. \tag{3.4}$$

Phase space diagrams provide one tool for assessing the flow state. Namely, traces which converge to a single point are steady state, those which repeat the same values periodically are simply transient, and those which display non-repeating behavior are chaotic. Put another way, the random aspect of post-transition flows are identified when an arbitrarily large number of terms can be included in a predictive model without achieving arbitrarily accurate solutions for any later time.

https://doi.org/10.4208/aamm.OA-2016-0103 Published online by Cambridge University Press

4 Results

4.1 Verifying MRT-iLBM with steady LDC flow

Steady-state results from the MRT-iLBM method at three Reynolds numbers are compared with literature results in order to check the correctness of the MRT-iLBM code. Table 1 shows the x and y velocity components of the MRT-iLBM computations and the same from recent literature. Additionally the resultant velocity components are listed, and the percent difference between literature and MRT-iLBM resultant velocities are shown to be small, less than 0.15% for the three Reynolds numbers considered.

Fig. 3 provides a more complete picture of the velocity profile comparison for Re 1,000. Both x and y velocity components are plotted for both MRT-iLBM and literature results. The good agreement between the two demonstrates both accuracy of the MRT-iLBM and adequacy of the lattice discretization to capture near-wall gradients.

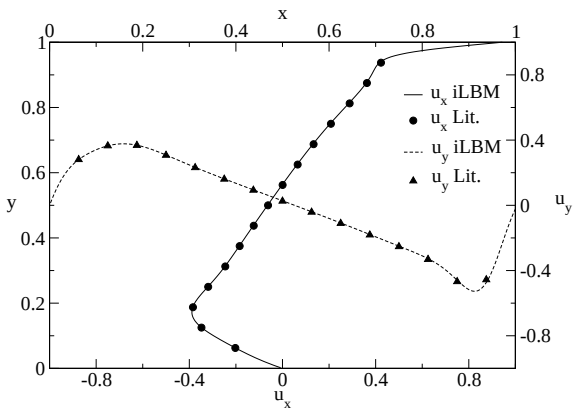


Figure 3: Re 1,000 velocity profiles: u velocity at $x = 0.5$, v velocity at $y = 0.5$, iLBM and Marchi et al. (see [13]).

The final point on steady laminar flow analysis is to compare the LBM-iMRT results to literature results on a comparable grid. Using the Marchi [13] result as the baseline for comparison, Table 2 shows that the current method produces comparable results (within 1.2%) on the coarser 100×100 grid. Thus, equivalence between this method and Navier-Stokes based codes for non-DNS simulations is demonstrated. Secondly, the minor difference in results between the coarser and finer grids using the present method show that the spacing criteria used produces grid independent results to within one percent.

4.2 The first Hopf bifurcation and transition to chaos

The first Hopf bifurcation point is the Reynolds number at which the flow changes from a steady solution to one which shows oscillatory behavior. Following the method of Cazemier et al. [5], the bifurcation point can be predicted by using the change in the

https://doi.org/10.4208/aamm.OA-2016-0103 Published online by Cambridge University Press

Table 1: Steady-State Predictions of iLBM Match Literature to within 0.2%.

Re	iLBM			[13]			$\|\boldsymbol{u}\|\%diff$
	u_x	u_y	$\|\boldsymbol{u}\|$	u_x	u_y	$\|\boldsymbol{u}\|$	
100	-2.091e-1	5.754e-2	2.169e-1	-2.091e-1	5.754e-2	2.169e-1	-0.003
400	-1.152e-1	5.206e-2	1.263e-1	-1.151e-1	5.206e-2	1.262e-1	0.081
1,000	-6.219e-2	2.578e-2	6.732e-2	-6.206e-2	2.580e-2	6.720e-2	0.176

Table 2: Comparison between literature and the current method on a coarse grid at Re 1,000.

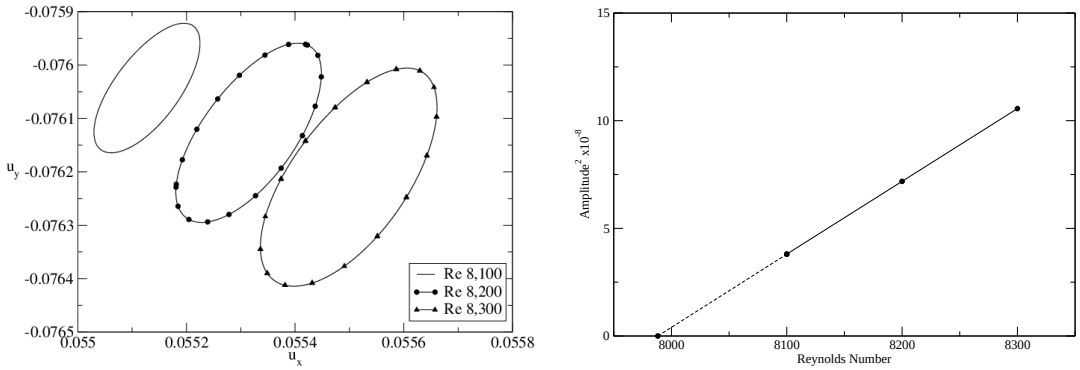
	u_x	u_y	$\|\boldsymbol{u}\|$	$\|\boldsymbol{u}\|\%diff$
Ghia [6] (129×129)	-6.080e-2	2.526e-2	6.584e-2	-2.02
Marchi [13] (1024×1024)	-6.205e-2	2.579e-2	6.720e-2	-
This work (coarse grid, 100×100)	-6.292e-2	2.565e-2	6.795e-2	1.12
This work (nominal grid, 178×178)	-6.219e-2	2.578e-2	6.732e-2	0.19

square of signal oscillation amplitude A^2_{amp} with Reynolds number to determine the point at which A^2_{amp} goes to zero. In this case A_{amp} was taken to be equal to the difference between maximum and minimum values of u velocity at point (0.6,0.6). Oscillation amplitudes were taken from MRT-iLBM simulations of flow at Re 8,100, 8,200, and 8,300 on grids of 854×854, 862×862, and 870×870 respectively. Fig. 4(a) shows the progression of the phase space plots in question. Potential sensitivity of oscillation amplitude to changes in the spatial discretization was checked by performing two simulations at Re 9,000. The first simulation used the nominal grid sizing of this work ($Re^{0.75}$ lattice sites in each direction–a 925×925 grid), and the second reduced the grid count by 25%. Oscillation frequency and amplitudes were identical between the two, whereas the mean was reduced by 0.3% in the lower resolution case. Through this, the $Re^{0.75}$ estimate was deemed as acceptable for grid independence.

Fig. 4(b) shows the linear interpolation based on the square of oscillation amplitude data from the three Reynolds numbers named above. As has been observed previously [5], the oscillation amplitude grows with the square of the Reynolds number beyond the first Hopf bifurcation, so the use of a linear interpolation based on the square is appropriate. The intersection of this curve fit equation with 0 oscillation amplitude was then taken as the first Hopf Bifurcation point for this case, and it is predicted to occur at Re 7,988 by the MRT-iLBM. This value is corroborated by the fact that the flow at Re 8,000 showed a nonzero but very small oscillating amplitude. Error was estimated by fitting a second order polynomial to data points at Re 8,100, 8,200, and 8,300 and computing the difference between the zero amplitude Reynolds number of that equation and the linear interpolation method. The Re_{Hopf} predicted by this second order polynomial is 8,007. This difference being indicative of the leading error term for the linear interpolation, the uncertainty of $\pm$ 19 is associated with the linear interpolation estimate of 7,988.

Table 3 summarizes literature which predicted the first Hopf bifurcation of the 2D lid driven cavity flow according to the method used and the reported Reynolds number of

https://doi.org/10.4208/aamm.OA-2016-0103 Published online by Cambridge University Press



(a) Phase Space Plots at point $(0.6,0.6)$

(b) Amplitude-interpolation method predicts $Re_{Hopf}=7{,}988$

Figure 4: Results for Re 8,100–8,300 and their use for predicting the onset of transience.

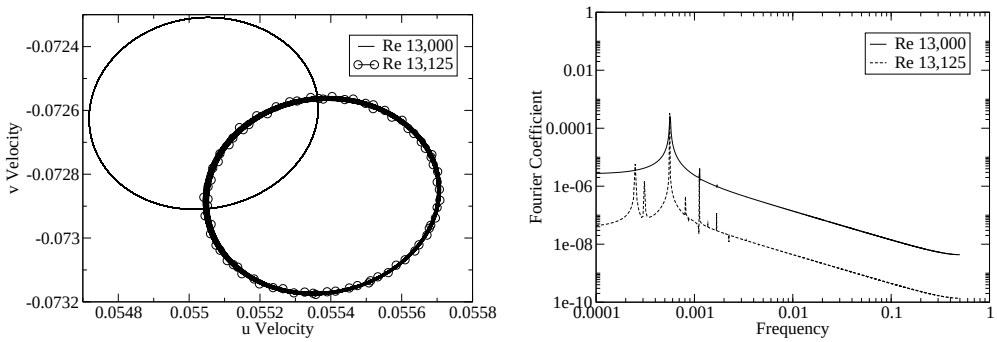
the bifurcation. The Re_{Hopf} result of this work agrees well with the prior DNS simulation of Cazemier et al. [5], and the Lyupanov stability analysis of Bruneau and Saad [3]. While within 4% of the previous results, the results of Peng et al. [18], Poliashenko and Aidun [19], and the POD-based prediction of Cazemier et al. [5] are somewhat lower than the value reported here. The POD method of Cazemier et al. was a valuable and informative exercise in mathematics but not useful as a tool for general flow analysis.

Peng et al. [18] embellishes upon the bifurcation behavior of the LDC flow solution at Reynolds numbers between Re_{Hopf} and the Re 11,000. It is known that the flow undergoes bifurcations to become two-periodic and then one-periodic as the Reynolds number is increased beyond the first Hopf bifurcation. Eventually stability conditions in the flow change such that perturbations are not damped out over time, but cause further flow perturbations. Transition to chaos is assessed by checking how faithfully the phase space traces repeat the same circuit. Fig. 5 shows the difference in phase space plots between two Reynolds numbers which lie on either side of transition. Both plots capture 1 million time steps and a few tens of characteristics times of the flow; the flow at Re 13,000 has perfect repeatability of the solution. Alternatively, Re 13,125 is identifiable as post-transitional because of the lack of any repetition in the phase space trace.

Table 3: Summary of literature Hopf bifurcation predictions for 2D lid driven cavity.

Reference	Methodology	Re_{Hopf}
[5]	Oscillation amplitude interpolation to zero, N-S DNS	7,972
[5]	POD model prediction by model constructed from Re 22k DNS results	7,819
[18]	Interpolation to zero amplitude, 200×200 grid, 6^{th} order inner, 2^{nd} order bc's	7,704
[19]	Direct dynamical system stability analysis	7,763
[3]	Lyapunov Stabilty Analysis	8,000–8,050
This Study	Interpolation to zero amplitude, MRT-iLBM DNS	$7{,}988 \pm 19$

https://doi.org/10.4208/aamm.OA-2016-0103 Published online by Cambridge University Press



(a) Phase Space Result (b) Frequency Spectrum Result

Figure 5: Results from point $(0.6,0.6)$ before transition (Re 13,000) and after (Re 13,125).

4.3 Post-transition statistics

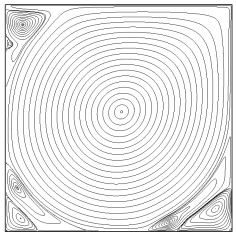
This section reports results of DNS simulations at two high, post-transition, Reynolds numbers: Re 15,000 and Re 20,000. Per the Kolmogorov length estimate, the Re 15,000 case was run on a 1356×1356 grid and the Re 20,000 case on a $1{,}682\times1{,}682$ grids with uniform lattice spacing and the halfway bounce back (HBB) boundary condition as shown in Fig. 2. Statistical results for mean flow, turbulence kinetic energy (2D version) (tke), turbulent energy dissipation ϵ (2D version), the Kolmogorov length scale η_k, and the anisotropy of the instabilities are presented.

Fig. 6 shows the statistical results from Re 15,000. Mean streamlines show good agreement with published results, including capture of the very small self-contained mean flow circulation zones in the bottom corners of the domain. ϵ shows high values near the top right corner of the domain where flow from the driven wall impinges upon the neighboring non-moving wall. Following mean streamlines, the tke does not show appreciable variation until the bottom wall is reached. This fact suggests that the very high dissipation rates in the upper right corner were keeping the tke magnitude low, and it is not until the bottom wall that tke production overcomes dissipation to produce notable tke values.

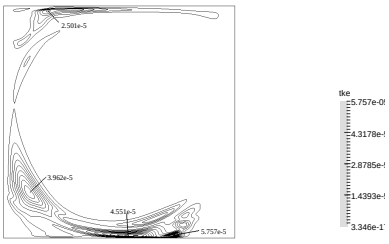
Kolmogorov lengthscale is another result in Fig. 6. The results tell that, relative to the grid length, the Kolmogorov length scale ranges from one-tenth of the grid spacing in busy areas to 271 times the grid spacing near the inactive domain center. A significant aspect of this result is the fact that, near the top and right side walls of the domain, the smallest scales of the flow are less than the scales which are being resolved by this analysis. Although somewhat displeasing, this result is in line with other DNS simulations which report grid spacing which is greater than the Kolmogorov length in very limited parts of the domain.

Fig. 7 shows time averaged coefficient of pressure in the domain, and the anisotropy ratio AR described in Section 3.1. Pressure coefficient shows typical trends; higher pres-

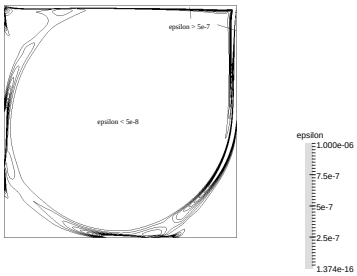
https://doi.org/10.4208/aamm.OA-2016-0103 Published online by Cambridge University Press



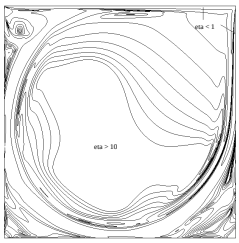
(a) Mean flow streamlines



(b) 2d-Turbulence kinetic energy

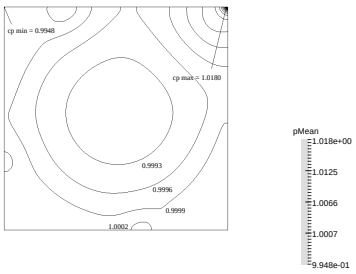


(c) 2d-Turbulence energy dissipation (ε) field

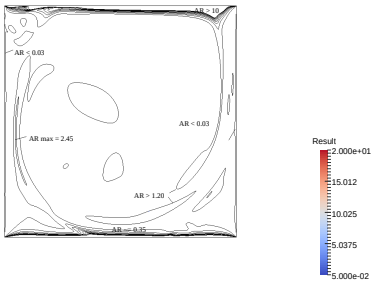


(d) Kolomogorov length scale (η_k) field (η_k, max = 271, η_k, min = 0.1)

Figure 6: Re 15,000 statistical property field contour plots.



(a) Pressure Coefficient



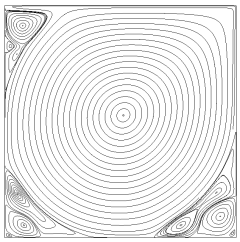
(b) Anisotropy Ratio

Figure 7: Statistical results for Re 15,000.

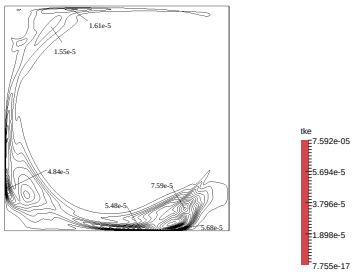
sure arises to turn the flow away from walls and corners, whereas low pressures exist in the center of flow features which involve circulation. This pressure field is noteworthy in that it comes from Eq. (2.8) which does not rely on a speed of sound.

Anisotropy Ratio, shown in Fig. 7, shows some trends not seen in simple flat plate turbulence. Anisotropy ratios greater than 1 indicate that the fluctuation in the x component of velocity is greater than than the fluctuation of the y component. As expected,

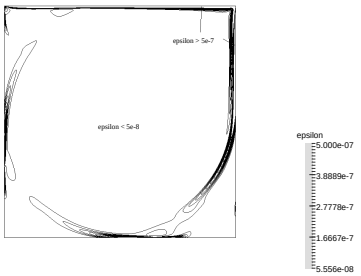
https://doi.org/10.4208/aamm.OA-2016-0103 Published online by Cambridge University Press



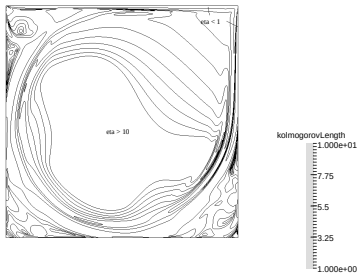
(a) Mean flow streamlines



(b) 2d-Turbulence kinetic energy



(c) 2d-Turbulence energy dissipation (ε) field



(d) Kolomogorov length scale (η_k) field (η_k, max = 235, η_k, min = 0.1)

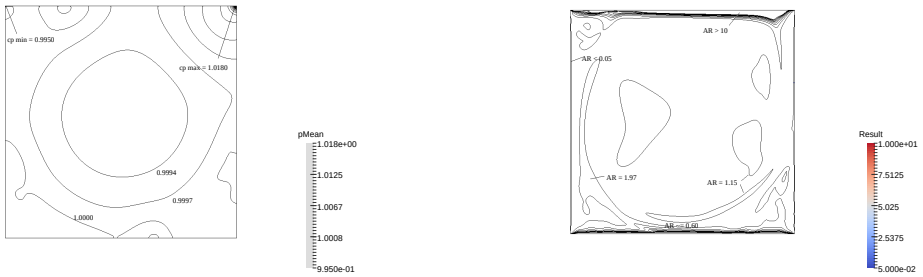
Figure 8: *Re* 20,000 statistical property field contour plots.

near-wall anisotropy ratios show that the dominant component of fluctuating velocity is from the component parallel to the wall, since the other component is dampened by the impermeability of the wall. Anisotropy ratio profiles on all non-driven walls show a reversal of the prevailing fluctuating velocity component in between the near-wall flow and the more calm flow in the domain center.

Statistical results for *Re* 20,000 are shown in Fig. 8. Streamlines of the mean flow show various self-contained circulation zones in the domain corners consistent with other literature results. A configuration of mean flow circulation zones similar to that of *Re* 15,000 results develops. Conceptually, increased diffusion of flow quantities due to turbulence-like mixing is clear when considering the mean flow streamlines of these cases. For example, the mean flow streamlines show tangential, shearing flow at the boundaries between circulation zones. This description leaves out the fact that the real flow has transient eddy features which convect flow across the mean flow streamline boundaries and enhance mixing. Mean flow energy loss is another side effect of the turbulence-like chaos which is not indicated by Figs. 6(a) and 8(a). Because the chaos, like turbulence, has no net time-averaged effect it constitutes a lower or "less useful" form of energy in the flow.

Energy dissipation rate results of Fig. 8(c) are similar to the *Re* 15,000 results, with high values on the driven wall and right hand wall. Also similar to the *Re* 15,000 re-

https://doi.org/10.4208/aamm.OA-2016-0103 Published online by Cambridge University Press



(a) Pressure Coefficient (b) Anisotropy Ratio

Figure 9: Statistical results for Re 20,000.

sults, the high dissipation tends to suppress overall tke until later in the flow, analogous to developing flow in a flat plate. The field of Kolmogorov length scale for Re 20,000 is qualitatively similar to that of Re 15,000. With the uniform grid spacing used, Kolmogorov length scales near the driven and right side wall are one tenth of the resolved length scales. Near the center of the domain where the flow is less active, the smallest flow features are approximated as 235 times larger than the resolved scales. As noted previously, DNS simulations typically have a small part of the domain which is under-resolved. It is noteworthy that the largest Kolmogorov scale in this case is smaller than that of Re 15,000–although Kolmogorov's theory says nothing of the largest scales. On the other hand, the fact that using $Re^{0.75}$ nodes in each direction leads the smallest computed η_k values in the two simulations to be the same agrees with Kolmogorov's theory that the smallest length scales are proportional to $Re^{-0.75}$.

Fig. 9 presents results for the pressure coefficient and anisotropy ratio. Both of these fields have analogous behavior to their Re 15,000 counterparts, with variation in magnitudes. Flow-turning high pressure zones are present in near corners and wall centers, while low pressure zones exist at centers of mean flow circulation. With this Re we have the ability to make some direct qualitative comparison with literature [22]. In the work of Zhang et al. [22], the similarity of the pressure field features is very similar, including how the pressure changes away for the corners, the main contour band shapes radiating from the center of the domain, and even the appearance of contour bands on the bottom at approximately x=0.6, on the left at approximately y=0.3, and the top at approximately x=0.2. Variations do appear, but this is expected as the work of Zhang et al. [22] uses the weakly compressible LBE and a coarser grid. Interestingly, their work presents a "viscosity counteracting" modification to the MRT form which has unique value in such high-Re simulation, and is considered for future work.

An interesting feature of these flows is the anisotropy ratio on the non-driven walls for both cases. Whereas flat plate turbulent flow anisotropy maintains the order of highest-to-lowest as a function of distance from the wall, the LDC unstable results presented here do not. Consider the bottom wall of Re 20,000. AR at the wall is much greater than

https://doi.org/10.4208/aamm.OA-2016-0103 Published online by Cambridge University Press

1 because u_2 is damped due to the presence of the wall, and this is consistent with flat plate statistics. For the LDC, however, away from the wall AR reaches values as low as 0.6. In this location the RMS fluctuating velocity component perpendicular to the wall is larger than the corresponding wall-parallel component. This trend differs from flat plate flow results.

5 Conclusions

We have utilized the relatively new incompressible lattice Boltzmann equation with a multiple relaxation time collision operator as a direct numerical simulation tool. Steady laminar to chaotic flow transition has been documented with comparisons to literature and attention drawn to interesting phenomena such as the anisotropy ratio throughout the field. As a steady laminar solver, the method is well established, but it is also clear the simulation of macroscopic flows experiencing instabilities and chaos is also well founded. The agreement of our method quantitatively at the first Hopf bifurcation with the majority of literature, and the qualitative agreement post-transition indicates that not only is the method valuable as a continuum flow solver, but also good resolution with a 2nd-order method may be more appropriate than a higher-order method with lower resolution. Future work interests include the viscosity counteracting modification to the MRT form for further high-Re benefits in the LBM.

Appendix

A D2Q9 incompressible MRT-LBE

Continuing from the work of Bouzidi et al. [2] the form of the evolution equation with MRT operator in velocity space $\mathbb{V}$ is,

$$\mathbf{f}(\mathbf{x}+\delta\mathbf{x},t+\delta t)=\mathbf{f}(\mathbf{x},t)-\mathbf{\Lambda}(\mathbf{f}-\mathbf{f}^{eq}), \tag{A.1}$$

and in moment space $\mathbb{M}$,

$$\mathbf{m}(\mathbf{x}+\delta\mathbf{x},t+\delta t)=\mathbf{m}(\mathbf{x},t)-\mathbf{S}(\mathbf{m}-\mathbf{m}^{eq}). \tag{A.2}$$

Defining

$$\mathbf{m}=(m_0,m_1,\cdots,m_8)^T \quad \text{and} \quad \mathbf{f}=(f_0,f_1,\cdots,f_8)^T \tag{A.3}$$

with the relationship

$$\mathbf{m}=\mathbf{M}\mathbf{f}. \tag{A.4}$$

https://doi.org/10.4208/aamm.OA-2016-0103 Published online by Cambridge University Press

For a square lattice ($a=1$), D2Q9 model the transformation matrix here takes the form:

$$\mathbf{M}=\begin{bmatrix}\boldsymbol{\psi}_0\\ \boldsymbol{\psi}_1\\ \boldsymbol{\psi}_2\\ \boldsymbol{\psi}_3\\ \boldsymbol{\psi}_4\\ \boldsymbol{\psi}_5\\ \boldsymbol{\psi}_6\\ \boldsymbol{\psi}_7\\ \boldsymbol{\psi}_8\end{bmatrix}=\begin{bmatrix}1&1&1&1&1&1&1&1&1\\ -4&-1&-1&-1&-1&2&2&2&2\\ 4&-2&-2&-2&-2&1&1&1&1\\ 0&1&0&-1&0&1&-1&-1&1\\ 0&-2&0&2&0&1&-1&-1&1\\ 0&0&1&0&-1&1&1&-1&-1\\ 0&0&-2&0&2&1&1&-1&-1\\ 0&1&-1&1&-1&0&0&0&0\\ 0&0&0&0&0&1&-1&1&-1\end{bmatrix}, \tag{A.5}$$

consisting of the row base vectors,

$$\begin{cases}\boldsymbol{\psi}_0=\|\boldsymbol{c}_i\|^0, & \boldsymbol{\psi}_3=c_{x,i}, & \boldsymbol{\psi}_6=c_{y,i}\|\boldsymbol{c}_i\|^2,\\ \boldsymbol{\psi}_1=3\|\boldsymbol{c}_i\|^2-4\|\boldsymbol{c}_i\|^0, & \boldsymbol{\psi}_4=c_{x,i}\|\boldsymbol{c}_i\|^2, & \boldsymbol{\psi}_7=c_{x,i}^2-c_{y,i}^2,\\ \boldsymbol{\psi}_2=\|\boldsymbol{c}_i\|^4, & \boldsymbol{\psi}_5=c_{y,i}, & \boldsymbol{\psi}_8=c_{x,i}c_{y,i},\end{cases} \tag{A.6}$$

each of which is orthogonalized, and thus every row of $\mathbf{M}$ is mutually orthogonal.

Collision matrices are related through

$$\mathbf{S}=\mathbf{M}\boldsymbol{\Lambda}\mathbf{M}^{-1}. \tag{A.7}$$

The moment collision matrix is diagonal with elements,

$$\mathbf{S}=[s_0,\ s_1,\ s_2,\ s_3,\ s_4,\ s_5,\ s_6,\ s_7,\ s_8], \tag{A.8}$$

giving viscosity,

$$\nu=c_s^2\left(\frac{1}{s_8}-\frac{1}{2}\right). \tag{A.9}$$

Equilibrium moments resulting from (A.4) applied to the standard FEQ (2.2) are:

$$\begin{cases}m_0^{eq}=\rho, & m_3^{eq}=\rho u_x, & m_6^{eq}=-\rho u_y,\\ m_1^{eq}=-2\rho+3\rho u^2, & m_4^{eq}=-\rho u_x, & m_7^{eq}=\rho(u_x^2-u_y^2),\\ m_2^{eq}=\rho-3\rho u^2, & m_5^{eq}=\rho u_y, & m_8^{eq}=\rho u_x u_y,\end{cases} \tag{A.10}$$

and applied to the incompressible FEQ ((2.7a) and (2.7b)):

$$\begin{cases}m_0^{eq}=0, & m_3^{eq}=u_x, & m_6^{eq}=-u_y,\\ m_1^{eq}=6P+3u^2, & m_4^{eq}=-u_x, & m_7^{eq}=u^2,\\ m_2^{eq}=-9P-3u^2, & m_5^{eq}=u_y, & m_8^{eq}=u_x u_y.\end{cases} \tag{A.11}$$

Moments resulting from (A.4) for the incompressible form are summarized as,

$$\mathbf{m}=\left[0,e,\epsilon,j_x,q_x,j_y,q_y,p_{xx},p_{xy}\right], \tag{A.12}$$

https://doi.org/10.4208/aamm.OA-2016-0103 Published online by Cambridge University Press

with physical significance: mass conservation, kinetic energy relation, kinetic energy relation squared, x momentum conservation, x energy flux relation, y momentum conservation, y energy flux relation, and diagonal and non-diagonal viscous stress relations, respectively.

Values on the diagonal of **S** have some freedom, but here are:

$$\mathbf{S}=\left[1,1.1,1,1,1.2,1,1.2,\frac{1}{\tau},\frac{1}{\tau}\right],\quad \nu=\frac{1}{3}\left(\tau-\frac{1}{2}\right). \tag{A.13}$$

Acknowledgments

The authors gratefully acknowledge the Michigan Technological University Computing & Visualization resource, Superior, which was the vehicle for performing these simulations.

References

[1] P. L. Bhatnagar, E. P. Gross and M. Krook, *A model for collision processes in gasses. I. Small amplitude processes in charged and neutral one-component systems,* Phys. Rev., 94 (1954), pp. 511–525.
[2] M. Bouzidi, D. d'Humieres, P. Lallemand and L. S. Luo, *Lattice Boltzmann equation on a two-dimensional rectangular grid,* J. Comput. Phys., 172 (2001), pp. 704–717.
[3] C. H. Bruneau and M. Saad, *The 2D lid-driven cavity problem revisited,* Comput. Fluids, 35 (2006), pp. 326–348.
[4] O. R. Burggraf, *Analytical and numerical studies of the structure of steady separated flows,* J. Fluid Mech., 24 (1966), pp. 113–151.
[5] W. Cazemier, R. W. Verstappen and A. E. Veldman, *Proper orthogonal decomposition and low-dimensional models for driven cavity flows,* Phys. Fluids, 10 (1998), pp. 1685–1699.
[6] U. Ghia, K. N. Ghia and C. T. Shin, *High-Re solutions for incompressible flow using the Navier-Stokes equations and a multigrid method,* J. Comput. Phys., 48 (1982), pp. 387–411.
[7] Z. Guo, B. Shi and N. Wang, *Lattice BGK model for incompressible Navier-Stokes equation,* J. Comput. Phys., 165 (2000), pp. 288–306.
[8] X. He, G. D. Doolen and T. Clark, *Comparison of the lattice Boltzmann method and the artificial compressibility method for Navier-Stokes equations,* J. Comput. Phys., 179 (2002), pp. 439–451.
[9] S. Hou, Q. Zou, S. Chen, G. Doolen and A. C. Cogley, *Simulation of cavity flow by the lattice Boltzmann method,* J. Comput. Phys., 118 (1995), pp. 329–347.
[10] P. Lallemand and L. S. Luo, *Theory of the lattice Boltzmann method: Dispersion, dissipation, isotropy, Galilean invariance, and stability,* Phys. Rev. E, 61 (2000), 6546.
[11] P. Lammers, K. N. Beronov and R. Volkert et al., *Lattice BGK direct numerical simulation of fully developed turbulence in incompressible plane channel flow,* Comput. Fluids, 35 (2006), pp. 1137–1153.
[12] J. Li and Z. Wang, *An alternative scheme to calculate the strain rate tensor for the LES applications in LBM,* Math. Problems Eng., (2010), 724578.

https://doi.org/10.4208/aamm.OA-2016-0103 Published online by Cambridge University Press

[13] C. H. MARCHI, R. SUERO AND L. K. ARAKI, *The lid-driven cavity flow: Numerical solution with a 1024×1024 grid,* J. Brazilian Society Mech. Sci. Eng., 31 (2009), pp. 186–198.
[14] S. MARIE, D. RICOT AND P. SAGAUT, *Comparison between lattice Boltzmann method and Navier-Stokes high order schemes for computational aeroacoustics,* J. Comput. Phys., 228 (2008), pp. 1056–1070.
[15] D. O. MARTINEZ, W. H. MATTHAEUS, S. CHEN AND D. C. MONTGOMERY, *Comparison of spectral method and lattice Boltzmann simulations of two-dimensional hydrodynamics,* Phys. Fluids, 6 (2006), pp. 1285–1298.
[16] G. R. MCNAMARA AND G. ZANETTI, *Use of the Boltzmann equation to simulate lattice-gas automata*, Phys. Rev. Lett., 61 (1988), 2332.
[17] J. R. MURDOCK AND S. L. YANG, *Alternative and explicit derivation of the lattice Boltzmann equation for the unsteady incompressible Navier-Stokes equation,* Int. J. Comput. Eng. Res., 6 (2016), pp. 47–59.
[18] Y. F. PENG, Y. H. SHIAU AND R. R. HWANG, *Transition in a 2-D lid driven cavity flow,* Comput. Fluids, 32 (2003), pp. 337–352.
[19] M. POLIASHENKO AND C. K. AIDUN, *A direct method for computation of simple bifurcations,* J. Comput. Phys., 121 (2006), pp. 246–260.
[20] B. SHI, N. HE AND N. WANG, *A unified thermal lattice BGK model for Boussinesq equations,* Prog. Comput. Fluid Dyn., 5 (2005).
[21] R. Z. WANG AND H. P. FANG, *Test of the possible application of the half-way bounce-back boundary condition for lattice Boltzmann methods in complex geometry,* Commun. Theor. Phys., 35 (2000), pp. 593–596.
[22] C. ZHANG, Y. CHENG, S. HUANG AND J. WU, *Improving the stability of the multiple-relaxation-time lattice Boltzmann method by a viscosity counteracting approach,* Adv. Appl. Math. Mech., 8 (2016), pp. 37–51.

https://doi.org/10.4208/aamm.OA-2016-0103 Published online by Cambridge University Press